Letter | Editors' Suggestion

Elucidation of the strong effect of an interfacial monolayer on magnetoresistance in giant magnetoresistive devices with current perpendicular to the plane

Björn Büker,[1,2] JinWon Jung,[1] Taisuke Sasaki,[1] Yuya Sakuraba,[1,*] Yoshio Miura,[1] Tomoya Nakatani,[1] Andreas Hütten,[2] and Kazuhiro Hono[1]

[1]*Research Center for Magnetic and Spintronic Materials, NIMS, 1-2-1 Sengen, Tsukuba, 305-0047 Ibaraki, Japan*

[2]*Department of Physics, Bielefeld University, Universitätsstraße 25, 33615 Bielefeld, Germany*

(Received 28 January 2021; revised 1 March 2021; accepted 17 March 2021; published 12 April 2021)

Electronic band matching at the interface between ferromagnetic (FM) and nonmagnetic (NM) metals has been considered a key factor that affects the spin-dependent transport properties such as giant magnetoresistance (GMR) effect. However, to date, there has not been an experimental explanation on the effect of a few monolayer atomic structures at the FM/NM interface on the band matching with a direct observation of the atomic- and element-resolved interfacial microstructure. In this study, we fabricated fully epitaxial current-perpendicular-to-plane GMR pseudo-spin-valve (PSV) films of half-metallic $Co_2FeGa_{0.5}Ge_{0.5}$(CFGG)/Ag spacer/CFGG structure with very thin (0 to 1 nm thick) Ni insertion layers at the CFGG/Ag interfaces. The MR ratio was significantly enhanced (from 23.1% for the PSV without Ni to 32.5% for that) with 0.21 nm-thick Ni insertion. Through an aberration-corrected scanning transmission electron microscopy (STEM), the state-of-the-art atomic-scale microstructure analysis revealed that the Co atoms in a second termination layer from the Ag interface are replaced with Ni monolayer via insertion of 0.21-nm-thick Ni. Our first-principles calculations of ballistic transmittance for the stacking structures modeled by the STEM images indicated that substituting the Co termination layer with Ni improved electronic band matching of majority spin electrons. This study proves that even a monolayer near the interface critically affects the interfacial band matching and MR properties.

DOI: 10.1103/PhysRevB.103.L140405

I. INTRODUCTION

The current-perpendicular-to-plane giant magnetoresistive (CPP-GMR) effect, which was originally observed in Ag/Co multilayers by Pratt *et al.* in 1991 [1], is one of the most thoroughly investigated phenomena in spintronics. Currently, owing to its promising applications in read heads [2–6] and spin-torque oscillators [7–10] for next-generation ultrahigh density hard disk drives and magnetic sensors [11], there is significant interest in CPP-GMR. Compared to the current-in-plane GMR effect, CPP-GMR has attracted much more interest in terms of fundamental spin-dependent transport [12,13]. This is because it is possible to interpret the spin-dependent transport more accurately. Valet and Fert have proposed a Boltzmann equation-based macroscopic expression for the CPP-GMR, considering the spin-diffusion length [14]. The Valet-Fert model treats spin-dependent scatterings using bulk and interfacial spin asymmetry coefficients, β and γ. This model predicts that higher magnetoresistance (MR) ratio is obtained by selecting a ferromagnetic (FM) material with a larger β and a suitable nonmagnetic (NM) spacer for larger γ. Recent studies have demonstrated large MR ratios of over 30% at room temperature (RT) in the CPP-GMR devices using half-metallic Co-based Heusler alloy layers, such as $Co_2FeGa_{0.5}Ge_{0.5}$ (CFGG) and an Ag spacer [15–19]. These large MR values are because of the large β and γ values originating from the half-metallicity of the Heusler alloys and good electronic band matching at the Heusler/Ag interfaces [17–19]. Recently, Jung *et al.* demonstrated a significant enhancement of the MR ratio to approximately 80% at RT in CFGG/Ag/CFGG structures with very thin 0.21-nm-thick (1.5 monolayers) NiAl insertion layers at the CFGG/Ag interfaces [20]. The reason for the enhancement of the MR ratio by NiAl insertion is unclear because the transmission electron microscopy (TEM) images taken for these samples do not give an element-resolved termination structure at the interface. However, it is presumed to be because of the enhancement of γ caused by the improvement of interfacial band matching by the presence of a NiAl layer at/near the interface.

The concept of the interfacial band matching in CPP-GMR has not been mentioned in the initial studies [1,14], where only spin-dependent scattering by interfacial defects and roughness has been considered. Schep *et al.* have calculated spin-dependent ballistic conductance in Co/Cu multilayers based on the local-spin-density approximation and predicted the importance of interfacial intrinsic band matching [21]. Subsequently, theoretical and experimental studies have confirmed that realistic electronic band matching is a crucial factor for CPP transport that determines the magnitude and sign of γ [22–25]. However, these studies did not investigate the effect of the atomic-level interfacial microstructure on the electronic band matching neither experimentally nor theoretically. Therefore, no one has ever experimentally

*Corresponding author: SAKURABA.Yuya@nims.go.jp

clarified whether a few monolayers at the FM/NM interface really affect band matching, to the best of our knowledge, and thereby influencing the MR properties of CPP-GMR devices.

In this study, to investigate the effect of atomic-scale interfacial structure on the banding matching and MR properties, we fabricated quality-controlled fully epitaxial CFGG/Ag/CFGG CPP-GMR devices with very thin Ni insertion layers at the CFGG/Ag interfaces. Since the microstructure analysis for previous devices with NiAl insertion revealed that a lot of Al atoms were diffused out from the NiAl layer, leaving a Ni-rich layer at one interface, Ni was selected as the insertion material [20]. To analyze how interfacial band matching varies with a structure and elements of few monolayers from the interface, we performed an atomic resolution microstructure analysis at the interface using scanning tunneling electron microscopy (STEM) and first-principles calculations of ballistic transmittance. The highest atomic resolution of elemental mapping images in earlier studies for any CPP-GMR devices proved the effect of just an interfacial monolayer on the band matching and MR property.

II. EXPERIMENTAL AND CALCULATION METHODS

Fully epitaxial (001)-oriented CPP-GMR pseudo-spin-valve (PSV) films consisting of CFGG (10 nm) /Ni(t_{Ni}) /Ag (5 nm)/Ni(t_{Ni}) /CFGG (10 nm) were prepared on a single crystalline MgO (001) substrate in an ultra-high vacuum magnetron sputtering system (base pressure is less than 3×10^{-7} Pa). To improve interfacial flatness in full stack of PSVs, Cr (10 nm) /Ag (100 nm) underlayers were deposited at ambient temperature and *in situ* annealed at 300 °C for 30 min. After CFGG/Ag/CFGG layers were grown at ambient temperature, the films were annealed *in situ* at 500 °C for 30 min to induce $L2_1$ atomic ordering in the CFGG layers. Ag (5 nm)/Ru (8 nm) capping layers were deposited after cooling the PSVs to ambient temperature. The CFGG layer was deposited from the $Co_{45.2}Fe_{22.6}Ga_{14.2}Ge_{18}$ alloy target using a RF power supply under Ar pressure (P_{Ar}) of 0.40 Pa with a deposition rate of 0.019 nm/sec. The Ni insertion layer and Ag spacer were deposited under $P_{Ar} = 0.40$ Pa and 0.66 Pa with the deposition rate of 0.014 and 0.045 nm/sec, respectively. The composition ratio of CFGG layers was determined to be $Co_{46.6}Fe_{23.4}Ga_{17.4}Ge_{12.6}$ using x-ray fluorescence analysis with the standard samples whose compositions were strictly evaluated with inductively coupled plasma mass spectrometry. We prepared five devices with different Ni insertion layer thicknesses: $t_{Ni} = 0$, 0.21, 0.42, 0.63, and 1 nm. The schematic stacking structure is shown in Fig. 1(a). The crystal structure and atomic order in the CFGG layers were characterized using x-ray diffraction (XRD). Through the high-angle annular dark-field scanning transmission electron microscopy (HAADF-STEM) and energy-dispersive x-ray spectroscopy (EDS) using an aberration-corrected STEM, FEI Titan G2 80–200, the microstructure around the CFGG/Ni/Ag spacer interfaces was observed. To measure the CPP-GMR properties, the PSV films were patterned into elliptical pillars with different sizes ranging from 300 × 150 nm to 80 × 40 nm. Afterward, the sidewalls of the pillars were insulated with SiO_2, and then the top and bottom electrodes were patterned using multiple UV-photolithography steps with Ta (2 nm) /Au (120 nm) layers to form four separate contacts for each pillar. The Ru surface of the capping layer was cleaned via Ar ion milling before depositing the top electrode. MR curves were measured via a DC four-probe method applying an external magnetic field to the longer axis of the elliptical pillars and a constant DC of 0.2 mA. The observed MR ratio (MR_{obs}) is defined as $(R_{AP}\text{-}R_P)/R_P$, where resistances R_P and R_{AP} are in parallel and anti-parallel states, respectively. The actual pillar size A was determined by observing the shape of pillars patterned on the reference CFGG/Ag/CFGG film using scanning electron microscopy. In addition, to calculate for RA, A for all the devices with different t_{Ni} was assumed to be the same.

The first-principles calculations for the ballistic conductance were performed using the QUANTUM ESPRESSO code package [26]. For the exchange-correlation energy, we adopted the ultrasoft pseudopotential method and the GGA [27,28]. Other details of the calculation method can be obtained from Ref. [29]. The stacking models for the calculation were constructed based on the actual interface structure observed via STEM. The in-plane lattice parameter of the supercell is fixed to be 4.06 Å, which corresponds to $a_0/\sqrt{2}$, where a_0 is the lattice constant of bulk CFGG (5.74 Å). The supercell includes 17 atomic layers of CFGG with the Ni and Co terminations and nine atomic layers of Ag (AgGa). The interfacial atomic structures were fully optimized for each interface according to the HAADF-STEM observations of the sample. Conductance calculations were implemented using an open quantum system, where the scattering equations were solved with semi-infinite boundary conditions, and the zero bias limit conductance at the Fermi level was obtained from the Landauer formula [30,31].

III. EXPERIMENTAL RESULTS

Figures 1(b) and 1(c) show the XRD pattern for the PSV films measured by changing the scattering vectors to the out-of-plane and ⟨111⟩ ($\chi = 54.7°$) directions of the CFGG layer, respectively. In the out-of-plane direction profile, only the (00l) plane is observed in the Cr, Ag, and CFGG layers, suggesting (001)-oriented fully epitaxial growth of all the PSV films for different Ni layer thicknesses. The inserted Ni layers were too thin to be detected via XRD. Although the lattice constant of bulk fcc Ni does not match that of Ag and CFGG at all, it is interesting to see that even the 1-nm-thick Ni insertion preserves (001)-oriented fully epitaxial growth. It is reported that even 3.5-nm-thick Ni thin film can be epitaxially grown in the metastable bcc structure with the lattice constant of 0.281 nm on the GaAs substrate. [32] Therefore, a formation of bcc structure in Ni insertion layers can be a reason for a fully epitaxial growth even with the 1-nm-thick Ni due to high lattice matching among CFGG, Ag and bcc Ni. The 002 superlattice peak from the CFGG layers, indicating $B2$ ordering like atomic ordering between Co and (Fe, Ga, and Ge), is detected in all the films. Because the 004 peak from CFGG overlaps with the 002 peak of the Cr buffer, reliable quantitative analysis of the degree of $B2$ order from the integrated intensity ratio of I_{002}/I_{004} from the profiles is

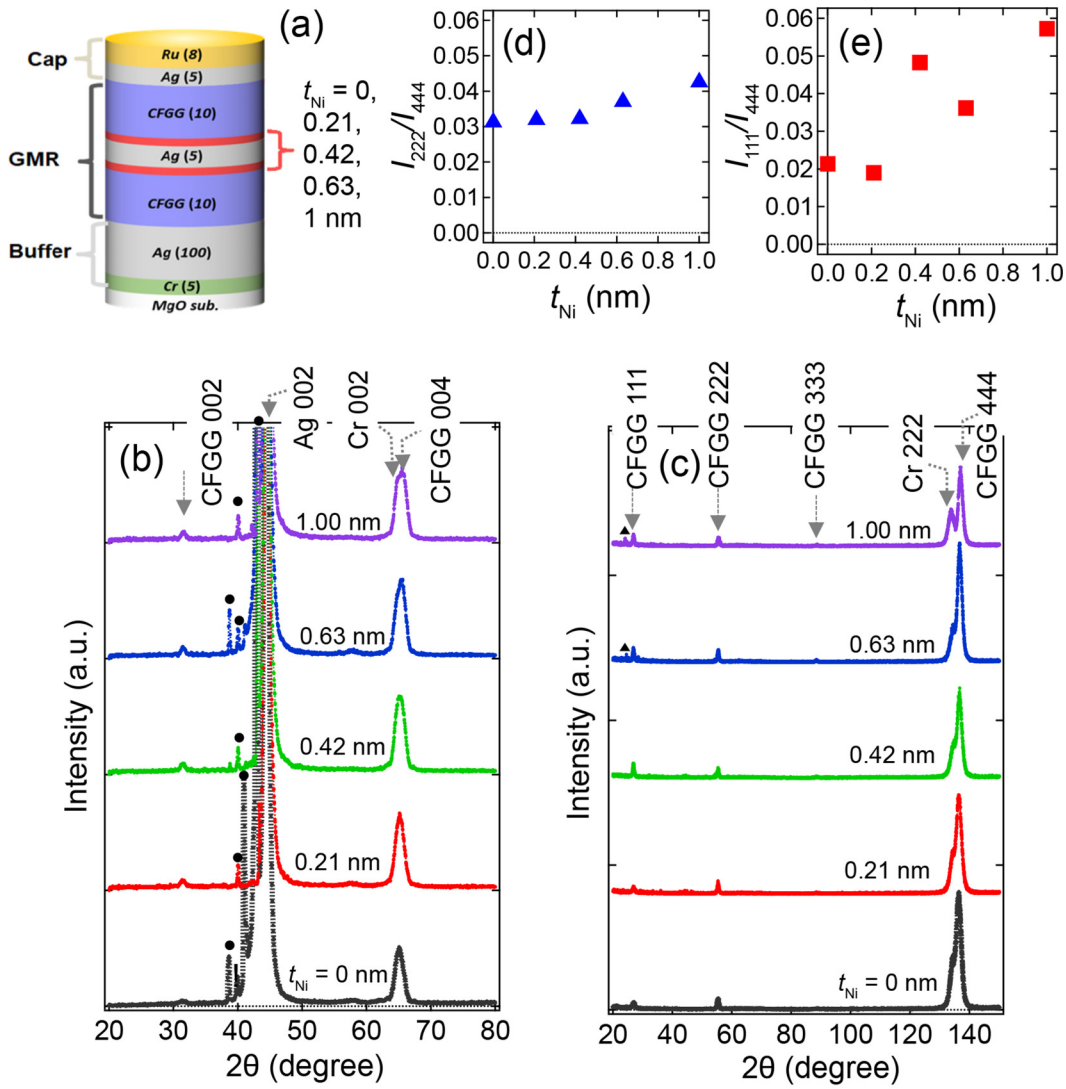

FIG. 1. (a) The schematic stacking structure of PSV films grown, (b), (c) θ-2θ scan for the PSV films having different t_{Ni} measured against out-of-plane ($\chi = 0^\circ$) direction and $\langle 111 \rangle$ ($\chi = 54.7^\circ$) direction of the CFGG layer, respectively. The peaks marked by • arise from the diffraction from MgO substrate. (d), (e) t_{Ni} dependence of I_{222}/I_{444} and I_{111}/I_{444}, respectively. The error bar of the data is smaller than the symbol size.

difficult. In the profile from the $\langle 111 \rangle$ direction, we observe 111 and 222 superlattice peaks in all the PSV films originating from $L2_1$ (the atomic order between Fe and (Ga,Ge))and $B2$ order. Because the 444 fundamental peak from the CFGG layers appears at very high 2θ over 135 °, well separated from the 222 peak of Cr, we estimated its integrated intensity and evaluated the intensity ratios of I_{222}/I_{444} and I_{111}/I_{444} to observe the t_{Ni} dependence of the $B2$ and $L2_1$ order on the CFGG layers, respectively [Figs. 1(d) and 1(e)]. Although I_{222}/I_{444} that reflects the degree of $B2$ order is nearly stable against t_{Ni}, we observed a scattering of I_{111}/I_{444} reflecting the degree of the $L2_1$ order. As shown later, our microstructure analysis detected the interdiffusion of the Ni layers to CFGG for $t_{Ni} = 0.63$ nm. Therefore, Ni interdiffusion in the thick t_{Ni} region might be a reason for the scattering of I_{111}/I_{444}. We also found an unexpected peak at around 24° only for $t_{Ni} = 0.63$ and 1 nm as indicated by the triangle mark in Fig. 1(c). However, herein, we should emphasize that both I_{222}/I_{444} and I_{111}/I_{444} are almost constant for the two PSV films with $t_{Ni} = 0$ and 0.21 nm, from which we observed a clear difference in the MR property as mentioned below.

Figures 2(a) shows the observed ΔR as a function of resistance in the parallel magnetization state (R_p) in the CPP-GMR PSVs with various designed pillar sizes for $t_{Ni} = 0$ and 0.21 nm. As shown in the inset of Fig. 2(b), the clear plateau resistance state of the antiparallel magnetization configuration was confirmed in the R–H curves for all the data points. The data are well fitted in the linear equation $\Delta R = aR + b$, from which the slope a gives an intrinsic MR (MR_{int}) free from the parasitic resistance (R_{para}) and the value of R_p obtained by extrapolating ΔR to zero gives R_{para}. Notably, the linear fitting of ΔR vs R_p can give us more accurate MR_{int} and R_{para} than that of R_p vs $1/A$ performed in previous studies in which the uncertainty of A gives an unavoidable error [15–19] because both ΔR and R_p are the electrically measurable values for each device with negligible experimental error. As confirmed by XRD, regardless of very similar atomic ordering in the CFGG layers between them, the slope of the fitting curve for

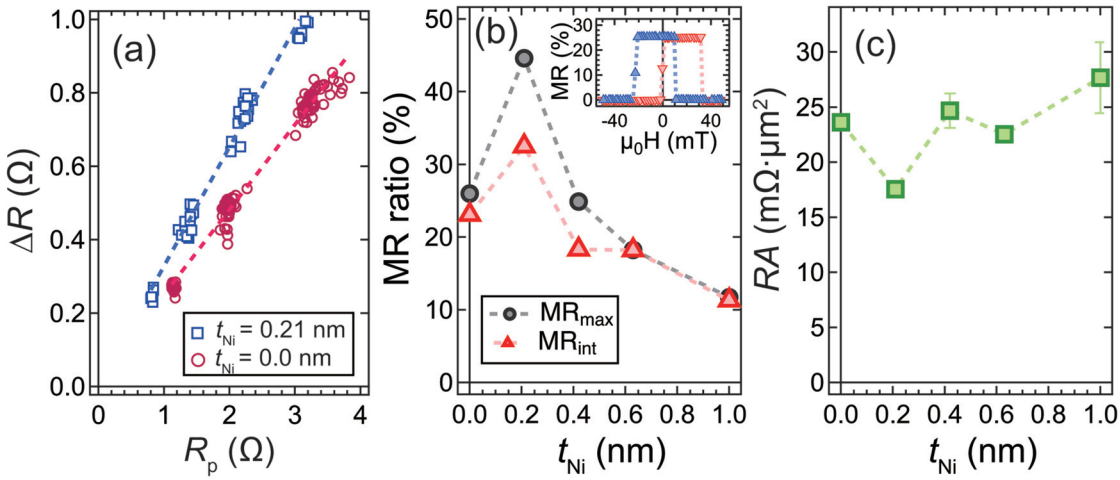

FIG. 2. (a) The R_p dependence of ΔR for the PSVs with $t_{Ni} = 0$ and 0.21 nm, (b),(c) The t_{Ni} dependence of MR ratio and RA, respectively. MR_{int} is the value obtained by the fitting of ΔR vs R_p. MR_{max} is the observed highest MR ratio. The inset of (b) is the typical MR loops, in which we clearly confirmed the plateau resistance in AP state.

$t_{Ni} = 0.21$ nm is larger than that for $t_{Ni} = 0$ nm. R_{para} was estimated to be almost zero in both samples. We observed that MR_{int} was enhanced from 23.1% to 32.5% by inserting 0.21-nm-thick Ni layers at the CFGG/Ag interfaces. In addition, the maximum observed MR ratio (MR_{max}) improved from 26.0% for $t_{Ni} = 0$ nm to 44.6% for $t_{Ni} = 0.21$ nm. The t_{Ni} dependence of MR_{int} and MR_{max} is shown in Fig. 2(b). It is observed that MR_{int} and MR_{max} largely enhanced only at $t_{Ni} = 0.21$ nm and then gradually decreased with increasing Ni thickness. As observed in the microstructure analysis mentioned below, the rapid decline in MR ratio for thicker Ni insertion ($t_{Ni} \geqslant 0.42$ nm) could be because of the interdiffusion of a part of the Ni layers toward the CFGG layers. The MR_{max} and MR_{int} are overlapped only for $t_{Ni} = 0.63$ and 1.00 nm because of less scattering of ΔR vs R_p, which could be due to better homogeneity of the interfacial microstructure than the samples with thinner Ni insertion. Additionally, the intrinsic RA was evaluated using a slope of R_p vs $1/A$ curve plotted in Fig. 2(c) although it may include a certain level of error owing to the uncertainty of the actual device size A. Interestingly, $R_{int}A$ clearly drops from 23.6 mΩ μm^2 in $t_{Ni} = 0$ nm to 17.6 mΩ μm^2 in $t_{Ni} = 0.21$ nm.

Figures 3(a)–3(c) show cross-sectional HAADF-STEM images and EDS elemental maps of Ag, Fe, Ni, and Ru obtained from the CPP-PSV films at $t_{Ni} = 0$, 0.21, and 0.63 nm, respectively. The Ag ($Z = 47$) and Ru ($Z = 44$) layers are brightly imaged with respect to the CFGG layers consisting of Co ($Z = 27$), Fe ($Z = 26$), Ga ($Z = 31$), and Ge ($Z = 32$) because the imaging contrast in the HAADF-STEM image depends on the atomic mass. The HAADF-STEM images show CFGG and Ag layers with sharp and flat interfaces. The cross-sectional EDS elemental map and the corresponding line concentration profile in Fig. 3(a) show that the constituent elements exhibit sharp compositional variations at the interfaces, indicating no noticeable interdiffusion in the sample without Ni insertion. In contrast, the Ni insertion layers are diffused within the CFGG layers, whereas this is not the case for the other constituent elements [Figs. 3(b) and 3(c)]. The EDS elemental map and the corresponding line concentration profile indicate that Ni is segregated at the Ag buffer layer/lower-CFGG and upper-CFGG/Ag capping layer interfaces in both the samples with $t_{Ni} = 0.21$ and 0.63 nm. Although a negligible amount of Ni was dissolved in the CFGG layers for $t_{Ni} = 0.21$ nm [Fig. 3(b)], Ni is inhomogeneously enriched in the dark imaged area in the CFGG layers for $t_{Ni} = 0.63$ nm [Fig. 3(c)]. Therefore, because the Ni atoms are expected to occupy the Co -site in the CFGG, such Ni dissolution in the CFGG layers causes small MR ratio due to the reduction of the bulk spin polarization β in the CFGG layers.

A high-magnification HAADF-STEM image and EDS elemental maps around the CFGG/Ag spacer interface regions for $t_{Ni} = 0$ nm are shown in Fig. 4. Note that these images are taken from the zone axes of $[100]_{Ag}$ and $[110]_{CFGG}$. Atomically sharp interfaces are observed at the CFGG/Ag interfaces. The atomic-resolution HAADF-STEM image [Fig. 4(a)] shows the $L2_1$-ordered structure in the CFGG layers. In the $L2_1$-ordered CFGG, Co, Fe, and Ga/Ge atoms are projected as individual atomic columns when they are observed from the $[110]_{CFGG}$ zone axis. Because of their larger atomic masses, Ga ($Z = 31$) and Ge ($Z = 32$) are brightly imaged compared to Fe ($Z = 26$). Since the brightly and darkly imaged atomic columns are arranged alternately within the Fe, Ga, and Ge layers, the formation of the $L2_1$ ordered structure is visually evident. Additionally, the atomic resolution EDS elemental maps show the structure of the CFGG/Ag interfaces [Figs. 4(b) and 4(c)]. For simplicity, the first, second, and third atomic layers from the pure Ag are defined as the first, second, and third termination layers (TLs), respectively [Fig. 4(d)]. As indicated by arrows [Figs. 4(b) and 4(c)], the EDS elemental map shows that the Ga-rich layers are present as the first TLs at both the upper and lower CFGG/Ag interfaces. Considering the imaging contrast in the HAADF-STEM image, as observed in a previous study, Ga and Ag atoms are almost alternately arranged in the Ga-rich first TLs [20]. The second TL consists of Co and Fe and (Ga/Ge) atoms are alternatively arranged in the third TL, which means that the $L2_1$ ordered CFGG layer is formed after the second TL. Based on these

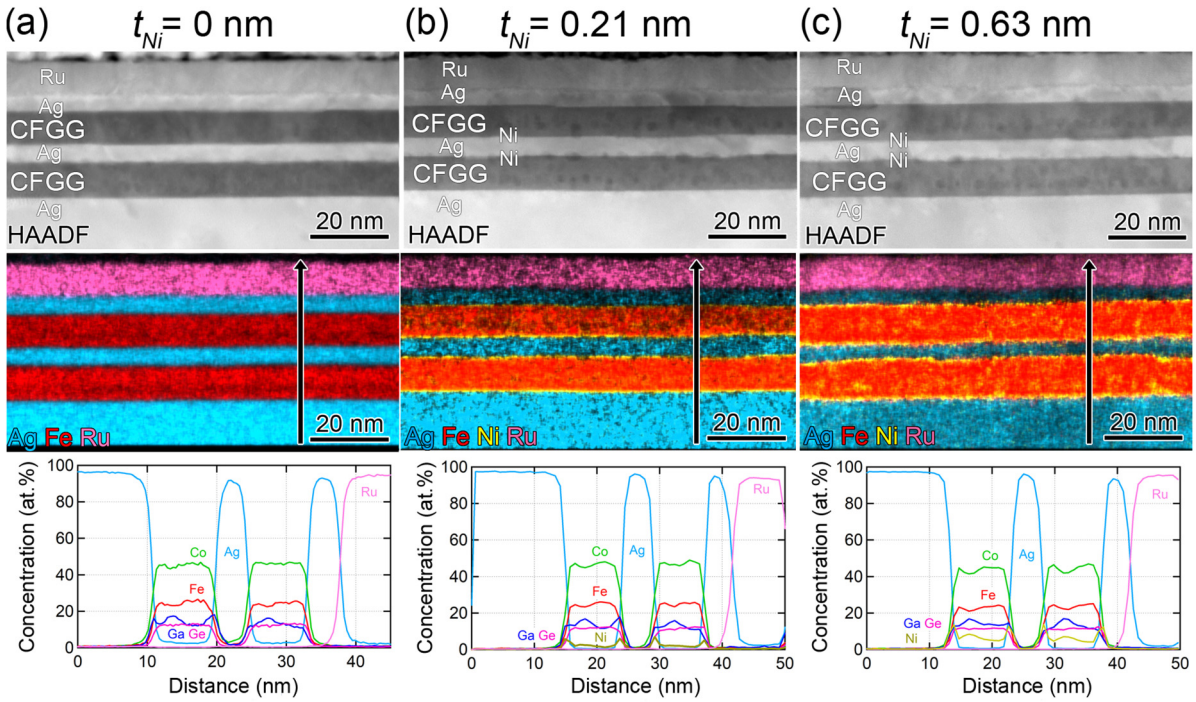

FIG. 3. (a)–(c) Low-magnification cross-sectional HAADF-STEM images, EDS elemental maps of Ag, Fe, Ni, and Ru and EDS line concentration profiles for constituent elements obtained from the PSV films with t_{Ni} = (a) 0, (b) 0.21, and (c) 0.63 nm, respectively. Note that the arrows in the EDS elemental maps show the analysis directions for the line profiles.

results, as schematically shown in Fig. 4(d), the interfacial structure for $t_{Ni} = 0$ nm can be determined. It should be noted that we found from the wider region of the STEM image near Ag interface that two steps terrace appears at a few points of Ag interface as we can see at the upper interface of Ag spacer in Fig. 4(a). However, we confirmed this two steps terrace does not break the termination structure shown in Fig. 4(d) schematically.

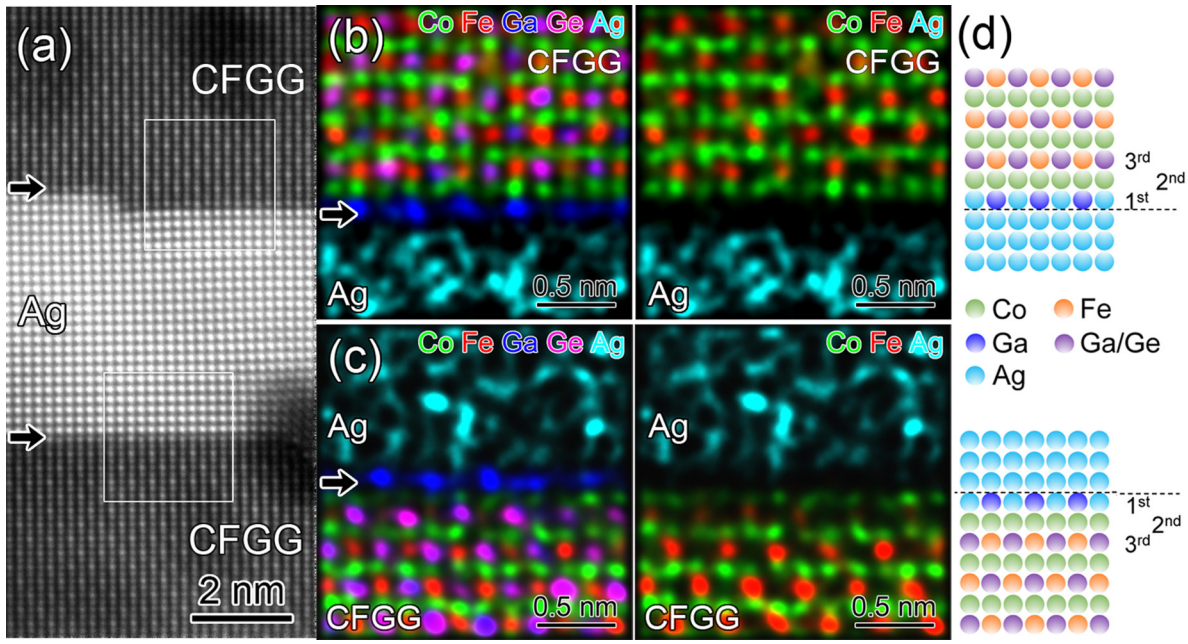

FIG. 4. (a) High-magnification HAADF-STEM images for the PSV without Ni insertion. Atomic-resolution EDS elemental maps of Co, Fe, Ga, Ge, and Fe for the (b) upper and (c) lower CFGG/Ag interfaces, respectively. Arrows in (a)–(c) indicate the first TLs in the sample, respectively. (d) The schematic illustration of the upper and lower CFGG/Ag interface structure constructed based on the STEM/EDS observations.

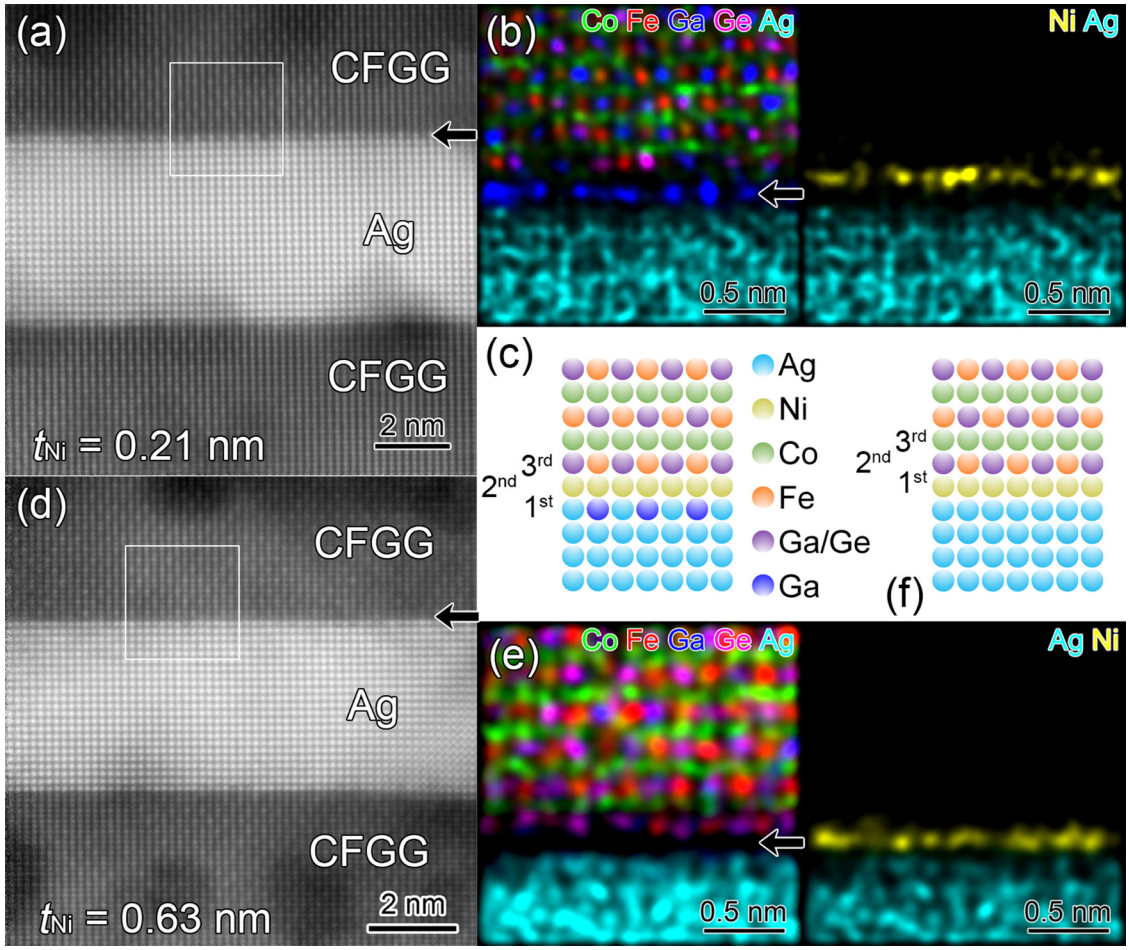

FIG. 5. (a) High-magnification HAADF-STEM image, (b) EDS elemental maps obtained from the area surrounded by a box in (a), and (c) schematic illustration of the interface structure for the sample with $t_{Ni} = 0.21$ nm. (d) High magnification HAADF-STEM image, (e) EDS elemental maps showing the elemental distribution in the area surrounded by a box in (d), and (f) Schematic illustration of the interface structure for the sample with $t_{Ni} = 0.63$ nm.

Figure 5 shows the HAADF-STEM images of the PSV films at $t_{Ni} =$ (a) 0.21 and (d) 0.63 nm, respectively. Although Ni was inserted at the Ag/CFGG interfaces, the EDS elemental map shows that a monoatomic Ni layer is formed in the second TL in the sample with $t_{Ni} = 0.21$ nm [Fig. 5(b)]. As observed in the sample without Ni insertion (Fig. 4), Ga and Ag atoms are alternately arranged in the first TL for $t_{Ni} = 0.21$ nm. The third TL consists of a Fe/(Ga,Ge) layer whose atomic columns are alternately arranged because of the $L2_1$ structure. As illustrated in Fig. 5(c), the insertion of Ni with $t_{Ni} = 0.21$ nm substituted Co with Ni in the second TL. Moreover, the CFGG layers in the sample with $t_{Ni} = 0.63$ nm have the $L2_1$ structure based on the HAADF image. However, unlike the samples with $t_{Ni} = 0$ and 0.21 nm, insertion of thicker Ni with $t_{Ni} = 0.63$ nm leads to the absence of the Ga/Ag layer in the first TL; the first TL of the sample with $t_{Ni} = 0.63$ nm is a monoatomic Ni layer. As expected from the $L2_1$-ordered structure of the CFGG layer, the second and third TLs are Fe/(Ga,Ge) and Co layers. It should be mentioned here that Ni atoms in the CFGG layer cannot be detected in this magnified EDS image for $t_{Ni} = 0.63$ nm, which might be due to the inhomogeneous distribution of Ni and its small concentration. We confirmed that both the upper and lower interfaces have a similar TL for each $t_{Ni} = 0.21$, 0.63 nm, and 0 nm.

IV. DISCUSSION

Herein, we discussed the effect of Ni insertion at the CFGG/Ag/CFGG interfaces on spin-dependent CPP transport by focusing on two PSVs with $t_{Ni} = 0$ nm and 0.21 nm. As shown in Fig. 2, a PSV with 0.21-nm thick Ni insertion exhibits a MR ratio that is 1.4 times as large as that of a PSV without Ni insertion. The XRD measurement confirms that the degree of $B2$ and $L2_1$ long-range order in the CFGG layers in the two PSVs are almost comparable, indicating a negligible contribution of β to the difference in MR ratios of these two PSVs. Low magnification TEM images show sharp and flat interfaces in both PSV films. Therefore, it can be speculated that the difference in the interfacial structure of TLs is attributable to the change in the MR ratio between them. To elucidate the difference in interfacial contribution in terms of electronic band matching, we performed first-principles calculations of ballistic conductance based on the actual

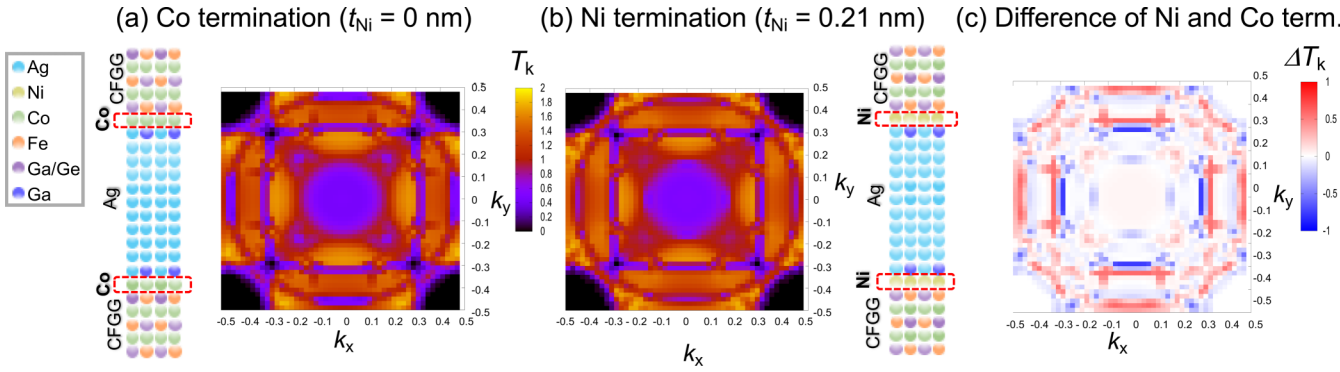

FIG. 6. (a), (b) The calculated in-plane k-vector ($k_{//}$) dependence of the ballistic transmittance of majority spin electron for the model constructed from the TEM images for the PSV with $t_{Ni} = 0$ and 0.21 nm, respectively. (c) The difference in the transmittance between (b) second Ni TL and (a) second Co TL cases.

atomic-resolved interfacial structure observed in the STEM images. Figures 6(a) and 6(b) show the calculated in-plane k ($k_{//}$) vector dependence of the majority spin electron transmittance for the structures with Co and Ni in the second TL cases as exhibited by the STEM analysis for $t_{Ni} = 0$ nm and 0.21 nm, respectively. Although it is difficult to visually recognize the difference in $k_{//}$ dependence of transmittance between Ni and Co second TL cases, the calculated theoretical interfacial resistance $R^{\uparrow}_{CFGG/Ag}A$ is smaller in the case with Ni second TL ($4.36\,m\Omega\,\mu m^2$) compared to that with Co second TL ($4.56\,m\Omega\,\mu m^2$). As shown in Fig. 6(c), through calculating the difference between the two cases, the $k_{//}$ regions showing higher transmittance with Ni second TL become visible. Therefore, our first-principles calculation indicates that the Ni second TL enhances the transmittance of the majority spin electrons compared to the case with Co second TL, thus resulting in smaller $R^{\uparrow}_{CFGG/Ag}A$. The difference between Co termination and Ni termination in the $R^{\uparrow}_{CFGG/Ag}A$ can be explained by the difference in interface distance between Co-Ag and Ni-Ag. Because the atomic radius of Ni (1.286 Å) is smaller than that of Co (1.302 Å), the interface distance of Ni-Ag (2.72 Å) is slightly smaller than that of Co-Ag (2.74 Å). Thus, the wave-function overlap for the Ni termination is larger compared to that of the Co termination. Therefore, Ni termination has better band matching and thus the smaller interfacial resistance. Because of the absence of down-spin electrons in the CFGG at the Fermi level owing to its half-metallicity, it is difficult to calculate $R^{\downarrow}_{CFGG/Ag}A$ reliably and thus γ $(=(R^{\downarrow}_{CFGG/Ag} - R^{\uparrow}_{CFGG/Ag})/(R^{\downarrow}_{CFGG/Ag} + R^{\uparrow}_{CFGG/Ag}))$ cannot be theoretically evaluated. However, higher γ is accompanied by improvement of band matching for majority spin electrons, which has a dominant contribution to transport. Notably, we cannot observe the quantitative agreement of the decrease in RA from $t_{Ni} = 0$ to 0.21 nm [Fig. 2(c)] with the difference in the calculated $R^{\uparrow}_{CFGG/Ag}A$ with Co and Ni second TLs. This might be because of the estimation error of the pillar size A in the experiment. Because we assumed ideal continuous one monolayer of Ni for this theoretical calculation, which could be different from the actual sample and thus causes quantitative error. However, the drop of RA at $t_{Ni} = 0.21$ nm is also explained by the improvement of band matching qualitatively. Therefore, it is concluded that the observed increase of MR from $t_{Ni} = 0$ nm to 0.21 nm coincides with the theoretical calculation of the ballistic transmittance. It is worth mentioning that the highest observed MR ratio in this study is much lower than the previous report for the CFGG/Ag/CFGG with a NiAl insertion [20]. Because a lot of Al atoms are found to be diffused out from thin NiAl layer, we speculate that Ni or NiAl insertion does not cause such a large difference in MR ratio. In addition, because high $L2_1$-ordering is observed in the CFGG layers in both studies, we infer there is a reason for large difference in MR ratio caused by the different composition of CFGG layers; $Co_{46.6}Fe_{23.4}Ga_{17.4}Ge_{12.6}$ (the total valence electron number $N_V = 28.4$) in this study and $Co_{47.2}Fe_{25.9}Ga_{13.4}Ge_{13.5}$ ($N_V = 29.0$) in a previous study. Recently Goto *et al.* confirmed that the position of Fermi level shifts by the N_V and affects the half-metallic nature in the CFGG film through the systematic transport measurements and the analysis of electronic structure using the hard x-ray photoemission spectroscopy. [33] Thus, too much hole doping caused by less N_V in the present CFGG than the stoichiometry (29.5) could shift the Fermi level largely and results in smaller bulk spin polarization, which can be a main reason for a small MR ratio. Therefore, an optimization of the composition in CFGG is expected to lead to higher MR ratio with Ni insertion.

V. CONCLUSION

In this study, we fabricated fully epitaxial CPP-GMR PSVs consisting of $Co_2FeGa_{0.5}Ge_{0.5}$(CFGG)/Ni/Ag/Ni/CFGG with varying Ni thickness from 0 to 1 nm. Additionally, we investigated their MR properties and microstructures near the CFGG/Ag interface regions to elucidate the effect of a few interfacial monolayers on the electronic band matching and the resultant MR properties. The intrinsic MR ratio increased from 23.1% to 32.5% by inserting a 0.21-nm-thick Ni layer at the interface, while the RA of the device reduced. The XRD analysis of the degree of atomic order in the CFGG layers confirmed that there was no remarkable change between the two samples, indicating an almost equal contribution from the bulk spin polarization of the CFGG on the MR properties. Systematic high-resolution microstructure analysis using an

aberration-corrected STEM enabled us to visualize the clear difference in interfacial atomic structure between them. The second TL from the CFGG/Ag interface is composed of Co in the PSV film without Ni insertion but that is replaced with Ni via a 0.21-nm-thick Ni insertion. Improvement of electronic band matching because of Ni substitution has been theoretically confirmed by the first-principles calculation of the ballistic transmittance performed on the structure observed in the STEM images. Consequently, this study elucidated that even a single monolayer structure near the interface affects the electronic band matching, thereby influencing the spin-dependent transport properties and MR properties. This knowledge will be very important for designing an interfacial structure to obtain much higher MR properties and realize the practical applications based on GMR devices.

ACKNOWLEDGMENTS

The authors thank N. Kojima, B. Masaoka, and K. Suzuki for their technical support. This work was supported by a Grant-in-Aid for Scientific Research (S) (Grant No. 17H06152) from the Japan Society for the Promotion of Science (JSPS). B. B. acknowledges the NIMS Internship Program, the JSPS Summer Program, and the German Academic Exchange Service (DAAD).

[1] W. P. Pratt, S.-F. Lee, J. M. Slaughter, ' R Loloee, P. A. Schroeder, and J. Bass, Phys. Rev. Lett. **66**, 3060 (1991).
[2] M. Takagishi, K. Yamada, H. Iwasaki, H. N. Fuke, and S. Hashimoto, IEEE Trans. Magn. **46**, 2086 (2010).
[3] T. Nakatani, S. Li, Y. Sakuraba, T. Furubayashi, and K. Hono, IEEE Trans. Magn. **54**, 3300211 (2018).
[4] T. M. Nakatani, S. Mitani, T. Furubayashi, and K. Hono, Appl. Phys. Lett. **99**, 182505 (2011).
[5] M. J. Carey, S. Maat, S. Chandrashekariaih, J. A. Katine, W. Chen, B. York, and J. R. Childress, J. Appl. Phys. **109**, 093912 (2011).
[6] H. Yuasa, M. Yoshikawa, Y. Kamiguchi, K. Koi, H. Iwasaki, M. Takagishi, and M. Sahashi, J. Appl. Phys. **92**, 2646 (2002).
[7] J. Zhu and Y. Tang, IEEE Trans. Magn. **44**, 125 (2007).
[8] S. Bosu, H. Sepehri-Amin, Y. Sakuraba, S. Kasai, M. Hayashi, and K. Hono, Appl. Phys. Lett. **110**, 142403 (2017).
[9] W. Zhou, H. Sepehri-Amin, T. Taniguchi, S. Tamaru, Y. Sakuraba, S. Kasai, H. Kubota, and K. Hono, Appl. Phys. Lett. **114**, 172403 (2019).
[10] M. Igarashi, Y. Suzuki, and Y. Sato, IEEE Trans. Magn. **46**, 3738 (2010).
[11] T. Shiroyama, Y. Sakuraba, T. Nakatani, H. Sepehri-Amin, J. W. Jung, and K. Hono, J. Appl. Phys. **124**, 163910 (2018).
[12] J. Velev and Y. C. Chang, Phys. Rev. B **67**, 144425 (2003).
[13] G. Binasch, P. Grünberg, F. Saurenbach, and W. Zinn, Phys. Rev. B **39**, 4828 (1989).
[14] T. Valet and A. Fert, Phys. Rev. B **48**, 7099 (1993).
[15] T. Iwase, Y. Sakuraba, S. Bosu, K. Saito, S. Mitani, and K. Takanashi, Appl. Phys. Express **2**, 063003 (2009).
[16] Y. Sakuraba, M. Ueda, Y. Miura, K. Sato, S. Bosu, K. Saito, M. Shirai, T. J. Konno, and K. Takanashi, Appl. Phys. Lett. **101**, 252408 (2012).
[17] S. Li, Y. K. Takahashi, T. Furubayashi, and K. Hono, Appl. Phys. Lett. **103**, 042405 (2013).
[18] T. M. Nakatani, T. Furubayashi, S. Kasai, H. Sukegawa, Y. K. Takahashi, S. Mitani, and K. Hono, Appl. Phys. Lett. **96**, 212501 (2010).
[19] Y. Sakuraba, K. Izumi, T. Iwase, S. Bosu, K. Saito, K. Takanashi, Y. Miura, K. Futatsukawa, K. Abe, and M. Shirai, Phys. Rev. B **82**, 094444 (2010).
[20] J. W. Jung, Y. Sakuraba, T. T. Sasaki, Y. Miura, and K. Hono, Appl. Phys. Lett. **108**, 102408 (2016).
[21] K. M. Schep, P. J. Kelly, and G. E. W. Bauer, Phys. Rev. Lett. **74**, 586 (1995).
[22] C. Vouille, a. Barthélémy, F. Elokan Mpondo, a. Fert, P. Schroeder, S. Hsu, a. Reilly, and R. Loloee, Phys. Rev. B **60**, 6710 (1999).
[23] M. Stiles and D. R. Penn, Phys. Rev. B **61**, 3200 (2000).
[24] K. Nikolaev, P. Kolbo, T. Pokhil, X. Peng, Y. Chen, T. Ambrose, and O. Mryasov, Appl. Phys. Lett. **94**, 222501 (2009).
[25] Y. N. Qi and S. Zhang, Phys. Rev. B **65**, 214407 (2002).
[26] P. Giannozzi, S. Baroni, N. Bonini, M. Calandra, R. Car, C. Cavazzoni, D. Ceresoli, G. L. Chiarotti, M. Cococcioni, I. Dabo, A. Dal Corso, S. Fabris, G. Fratesi, S. de Gironcoli, R. Gebauer, U. Gerstmann, C. Gougoussis, A. Kokalj, M. Lazzeri, L. Martin-Samos, N. Marzari, F. Mauri, R. Mazzarello, S. Paolini, A. Pasquarello, L. Paulatto, C. Sbraccia, S. Scandolo, G. Sclauzero, A. P. Seitsonen, A. Smogunov, P. Umari, and R. M. Wentzcovitch, J. Phys.: Condens. Matter **21**, 395502 (2009).
[27] J. P. Perdew, K. Burke, and M. Ernzerhof, Phys. Rev. Lett. **77**, 3865 (1996).
[28] D. Vanderbilt, Phys. Rev. B **41**, 7892 (1990).
[29] Y. Miura, K. Abe, and M. Shirai, Phys. Rev. B **83**, 214411 (2011).
[30] H. . Choi and J. Ihm, Phys. Rev. B **59**, 2267 (1999).
[31] A. Smogunov, A. Dal Corso, and E. Tosatti, Phys. Rev. B **70**, 045417 (2004).
[32] C. S. Tian, D. Qian, D. Wu, R. H. He, Y. Z. Wu, W. X. Tang, L. F. Yin, Y. S. Shi, G. S. Dong, X. F. Jin, X. M. Jiang, F. Q. Liu, H. J. Qian, K. Sun, L. M. Wang, G. Rossi, Z. Q. Qiu, and J. Shi, Phys. Rev. Lett. **94**, 137210 (2005).
[33] K. Goto, L. S. R. Kumara, Y. Sakuraba, Y. Miura, I. Kurniawan, A. Yasui, H. Tajiri, Y. Fujita, Z. Chen, and K. Hono, Phys. Rev. Mater. **4**, 114406 (2020).